

Research Paper

Bio-orthogonal click-targeting nanocomposites for chemo-photothermal synergistic therapy in breast cancer

Jianan Qiao*, Fengchun Tian*, Yudi Deng, Yunkai Shang, Shijie Chen, Enhao Chang, Jing Yao✉

State Key Laboratory of Natural Medicines and Jiangsu Key Laboratory of Drug Stability of Biopharmaceuticals, Department of Pharmaceutics, China Pharmaceutical University, 24 Tongjiaxiang, Nanjing 210009, China.

*Authors contributed equally.

✉ Corresponding author: Tel.: +86-25-86185328; yaojing@cpu.edu.cn.

© The author(s). This is an open access article distributed under the terms of the Creative Commons Attribution License (<https://creativecommons.org/licenses/by/4.0/>). See <http://ivyspring.com/terms> for full terms and conditions.

Received: 2019.11.25; Accepted: 2020.03.08; Published: 2020.04.06

Abstract

Chemo-photothermal synergistic treatment has a high potential to complement traditional cancer therapy and amplify its outcome. Precision in the delivery of these therapeutic agents to tumor cells has been indicated as being key to maximizing their therapeutic effects.

Method: We developed a bio-orthogonal copper-free click-targeting nanocomposite system (DLQ/DZ) that markedly improved specific co-delivery of the chemotherapeutic agent doxorubicin and the photosensitizer zinc phthalocyanine to breast cancer cells *via* a two-step mechanism. In the first step, an azide-modified sugar (tetraacetylated N-azidoacetyl-D-mannosamine, Ac4ManNAz) was injected intratumorally for glycoengineering of the tumor cell surface. Subsequently, DLQ/DZ was administered to achieve tumor enrichment *via* bio-orthogonal copper-free click-targeting.

Results: During the first step in our experiments, high density azide groups (3.23×10^7 /cell) were successfully glycoengineered on the surface of tumor cells following Ac4ManNAz administration *in vitro*. Subsequently, the highly efficient bio-orthogonal click chemical reaction between receptor-like azide groups on tumor cells and DBCO on nanocomposites significantly enhanced the cellular uptake and tumor-specific distribution (4.6x increase) of the nanocomposites *in vivo*. Importantly, Ac4ManNAz+DLQ/DZ treatment augmented the anti-cancer effect of combined chemotherapy and PTT (96.1% inhibition rate), nearly ablating the tumor.

Conclusions: This bio-orthogonal click-targeting combination strategy may provide a promising treatment approach for surficial breast cancers.

Key words: nanocomposite, chemo-photothermal synergistic therapy, metabolic glycoengineering, bio-orthogonal click chemistry, breast cancer

Introduction

Over the past few decades, the benefits of phototherapy have been demonstrated as an anti-cancer treatment that is non-invasive, has high spatiotemporal precision (limited mainly to the irradiated site), and low side effects [1-5]. In particular, photothermal therapy (PTT) utilizes the near-infrared (NIR, 650-900 nm) laser irradiation on the tumor site to kill tumor cells by producing local

heat with the assistance of photosensitizers [6-10]. This strategy often contributes to very significant therapeutic effects in the early stage. However, the residual tumor cells surviving from uneven temperature distribution in the tumor tissues may lead to recurrence [11-13]. It has been reported that solid tumor chemotherapy in combination with PTT effectively kills the remaining tumor cells caused by

uneven temperature distribution or insufficient laser exposure during PTT [4, 14-17]. More importantly, PTT enables a superior delivery of drugs deep into the tumor *via* expanded endothelial gaps, improved vascular perfusion [18-21], and increases the tumor drug accumulation by enhanced vascular permeabilization [22]. PTT also enhances tumor sensitivity to chemotherapeutics [23-26]. As such, the combination of chemotherapy and PTT has been shown to complement and amplify therapeutic effects. Precise co-delivery of chemotherapeutic agents and photosensitizers to the tumor whilst avoiding off-target exposure is the key to achieving optimal efficacy [25]. Nevertheless, conventional targeting strategies [27] that rely on the interaction between nanocarriers and tumor-specific receptors often result in sub-optimal outcomes. The problem is linked to the limited and varied numbers of endogenous (e.g. protein-based) receptors displayed on tumor cells [28, 29].

Metabolic glycoengineering dresses tumor cells with artificial receptors. The engineering utilizes the intrinsic metabolism of cancer cells and forces cells to incorporate the chemical groups of non-native sugars, such as azide-containing mannosamine derivatives, into their surfaces [30-32]. The amount of unnatural sugars administered to the tumor cells can be adjusted to control the density of chemical groups on the cell surface [33, 34]. Moreover, the expression of chemical groups as artificial receptors could be manually controlled and exclusively presented on tumor cells [35], which helps to reduce toxic side effects. Subsequently, cyclooctyne-modified nanocarriers may bind to the tumor surface *via* highly specific bio-orthogonal copper-free click chemical reactions, thereby, efficiently and accurately delivering antitumor agents [36].

It was reported that the number of "receptor-like" azide groups produced on the tumor cell surface by metabolic glycoengineering was 100-times higher than the estimated number of endogenous receptors [37]. Furthermore, cellular uptake of cyclooctyne-modified nanoparticles [33] based on metabolic glycoengineering and click reaction in human lung cancer (A549) cells was increased in about 10-fold compared to the nanoparticles delivered *via* endogenous receptor-mediated targeting [38, 39]. Therefore, the combination of metabolic glycoengineering and bio-orthogonal click chemistry may provide a better instrument for tumor-targeted drug delivery.

In the current study, a bio-orthogonal click-targeting nanocomposite was constructed to enable the synchronous delivery of photothermal conversion agent (zinc phthalocyanine, ZnPc) and

chemotherapeutic drug (doxorubicin, DOX) to lesion sites and to realize synergistic combination therapy of PTT and chemotherapy. We have previously demonstrated that low molecular weight heparin (LMWH)-quercetin (Qu) conjugate (LQ) is an efficient carrier for drug delivery and inhibits the activity and expression of P-glycoprotein on tumor cells [40]. In this case, dibenzocyclooctyne (DBCO) modified LQ conjugates (DLQ) were synthesized and self-assembled into nanocomposites in aqueous medium to co-encapsulate DOX and ZnPc through hydrophobic and π - π stacking interactions (i.e. DLQ/DZ). Tetraacetylated N-azidoacetyl-D-mannosamine (Ac4ManNAz) was used to engineer azide-rich tumor cell surface. As illustrated in Scheme 1, *i.t.* injection of Ac4ManNAz into the tumor site glycoengineered a large number of receptor-like azide groups distributed on the tumor cell surface. Subsequently, DLQ/DZ which accumulated in tumor *via* tumor-specific enhanced permeability and retention (EPR) effect could bind to highly-expressed azide groups on surface of tumor cells through the bio-orthogonal copper-free click chemistry reactions after *i.v.* injection, facilitating their internalization into tumor cells effectively. Following this, the esterase or acidic tumor environment hydrolyzed the ester bond of DLQ to release both ZnPc and DOX. ZnPc was irradiated by NIR laser to induce the rise in temperature inside tumor cell [41] and trigger tumor cell protein denaturation and coagulative necrosis to cause irreversible apoptosis. Activated cell death mechanisms reduced tumor resistance to chemotherapeutic drugs. Synergizing with ZnPc, DOX was concentrated in cell nuclei, blocked DNA synthesis, and inhibited tumor cell proliferation [42, 43]. Thus, the targeted nanocomposite utilized the autologous metabolic mechanism of tumors to achieve the efficient delivery of photosensitizer and chemotherapeutic drug. The combined physical and chemical treatments markedly enhanced the antitumor efficacy of used drugs, meanwhile maintaining a promising safety profile in the animal model. In this study, tumor-targeting drug delivery and chemo-photothermal therapeutic efficacy of DLQ/DZ nanocomposites were evaluated *in vitro* and *in vivo*.

Materials and Methods

Materials

Low molecular weight heparin (100 IU mg⁻¹, MW 4500 Da) was provided by Nanjing University (Nanjing, China). Quercetin was purchased from Sanwei Pharmaceutical Co., Ltd (Shanghai, China). Dox was purchased from Kaifang Pharmaceutical

Technology Co., Ltd (Shanghai, China). ZnPc was obtained from Sigma-Aldrich (Shanghai, China). N-methylpyrrolidone (NMP), 1-Ethyl-3-(3-dimethylaminopropyl) carbodiimide (EDC) and N-hydroxysuccinimide (NHS) were obtained from Aladdin Biochemical Technology Co., Ltd (Shanghai, China). DBCO-Cy5 and Ac4ManNAz were purchased from Click Chemistry Tools (Scottsdale, USA). Cy5-NH₂ was purchased from Xi'an ruixi Biological Technology Co., Ltd (Shanxi, China). Other chemicals were of analytical grade and were used without further purification.

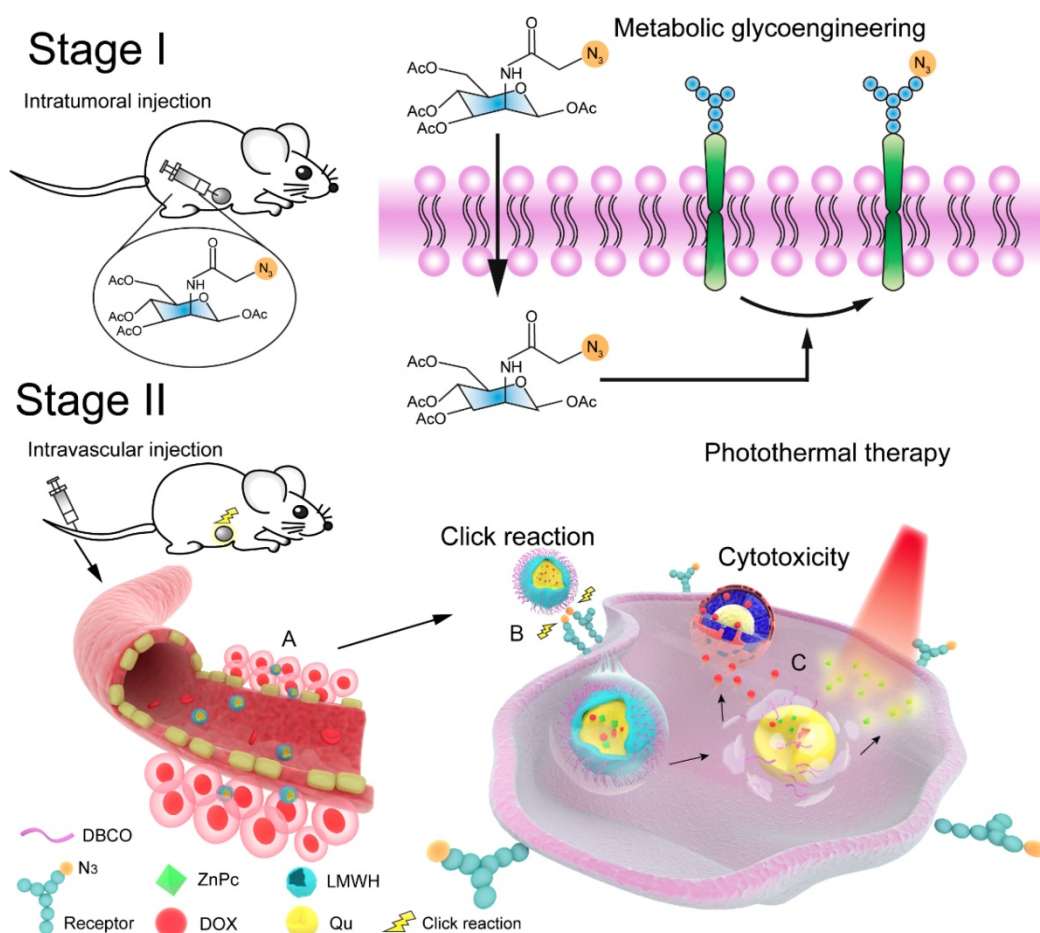
Synthesis and characterization of DLQ conjugates

DLQ conjugates were synthesized connecting Qu and DBCO into LMWH backbone *via* ester and amide bonds, respectively. DBCO-NH₂ synthesis method was reported in Supplementary Information section (Figure S1-7). Firstly, LMWH (1.0 mmol) was mixed to react with NHS (4.0 mmol) and EDC (4.0 mmol) in anhydrous formamide at 4 °C for 1 h. Afterwards, DBCO-NH₂ (2.0 mmol) solution was

added and mixture was stirred at 25 °C for 24 h. The reaction solution was quickly poured into subcooled acetone (5-10 volumes) and precipitated at -20 °C for 30 min. The precipitate was extracted by suction-forced filtration, dissolved in distilled water, and the resulting solution was dialyzed in MWCO=3500 dialysis bag for 2 days. DBCO-LMWH (DL) conjugates were obtained by lyophilization. The Qu was grafted onto the DL to obtain DLQ conjugates by the same method as the preparation of DL conjugates. The molar grafting ratio of DBCO (308 nm) and Qu (360 nm) into LMWH were calculated using UV-Vis spectroscopy according to the following formula.

$$\text{The molar grafting ratio (\%)} = (c / M_X) / [(m - c) / M_{\text{LMWH}}] \times 100\%$$

c was the content of Qu or DBCO, M_X was the molecular weight of Qu or DBCO, m was the mass of the conjugate, and M_{LMWH} was the molecular weight of a low molecular weight heparin structural unit.



Scheme 1. Schematic engineered of the click-targeting nanocomposites for chemo-photothermal synergistic therapy. Stage I: Production of azide groups on the surface of tumor cells by metabolic glycoengineering. Stage II: (A) Nanocomposites accumulated in tumor tissue through EPR effect. (B) Nanocomposites bound to tumor cell *via* bio-orthogonal copper-free click chemistry. (C) Chemotherapy combined with photothermal therapy to synergize anti-tumor by DNA damage of doxorubicin (DOX) and thermal ablation of zinc phthalocyanine (ZnPc) upon laser irradiation.

Various amounts of N-(2-aminoethyl)-2-azidoacetamide hydrochloride (10%, 20%, 30%, 50%, 70%) were added to the DLQ conjugate solution at room temperature for 2 h, and then subjected to lyophilization. The lyophilized products were ground with KBr, and then compressed. The infrared spectrum was recorded by infrared spectrometer (FT-IR Nicolet Impact 410). The degree of reaction between the azide group of N-(2-aminoethyl)-2-azidoacetamide hydrochloride and DBCO of DLQ was observed within FT-IR spectrum.

Synthesis of DLQ-Cy5

Cy5 was connected to DLQ *via* an amide bond. Firstly, DLQ (1.0 mmol) had been reacting with NHS (4.0 mmol) and EDC (4.0 mmol) in anhydrous formamide at 4 °C for 1 h. Following this, Cy5-NH₂ (2.0 mmol) solution was added and stirred at 25 °C for 24 h. Thereafter, the reaction solution was quickly poured into subcooled acetone (5-10 volumes) and precipitated at -20 °C for 30 min. The precipitate was extracted by suction-forced filtration, dissolved in distilled water. The solution was dialyzed in MWCO=3500 dialysis bag for 2 days. DLQ-Cy5 conjugates were obtained by lyophilization.

Preparation and characterization of DLQ/DZ nanocomposites

DLQ lyophilized product (18 mg) was dissolved in distilled water (3 mL) and slowly added 1.2 mL of DOX (5 mg/mL) solution (in DMF). The mixture was ultrasonicated for 30 min in an ice-filled bath. Following this, the resulting solution was dialyzed for 12 h and filtered through 0.8 µm filter to obtain the DLQ/DOX nanocomposites. Additionally, DLQ lyophilized product (18 mg) was dissolved in distilled water (3 mL) and slowly added 1.0 mL of ZnPc (3 mg/mL) solution (in NMP). The mixture was ultrasonicated for 30 min in an ice-filled bath. Afterwards, the resulting solution was dialyzed for 12 h and filtered through 0.8 µm filter to obtain the DLQ/ZnPc nanocomposites. Finally, DLQ lyophilized product (18 mg) was dissolved in distilled water (3 mL) and slowly added 1.2 mL of DOX (5 mg/mL) solution (in DMF) and 1.0 mL of ZnPc (3 mg/mL) solution (in NMP). The mixture was ultrasonicated for 30 min in an ice-filled bath. Following this, the resulting solution was dialyzed for 12 h and filtered through 0.8 µm filter to obtain the DLQ/DZ nanocomposites. To evaluate stability of drug-loaded nanocomposites, the particle size of drug-loaded nanocomposites (DLQ/DOX, DLQ/ZnPc and DLQ/DZ) was measured at 0, 0.5, 1, 2, 3, 4, 5, 6, 8, 10, 12, 24, 36, 48, 72, 96, and 120 h.

In vitro drug release profile

The kinetics of DOX release from DLQ/DZ nanocomposites was investigated using dialysis method *in vitro*. The dialysis bags containing equal amount DLQ/DZ nanocomposites (1 mg DOX) were placed in 200 mL PBS solution (pH 7.4, pH 5.8 or pH 4.5) and shaken at 100 rpm in a horizontal shaker (37 °C). Medium (1 mL) with released drugs was collected at different time points (0, 0.5, 1, 1.5, 2, 3, 4, 5, 6, 7, 8, 10, 12, 24, 36, 48, 72 h), then, 1 mL PBS was added.

In vitro photothermal conversion effect

The thermal profiles of DLQ/DZ in water were measured using 808 nm laser irradiation (FC-808-3000-MM, Changchun Ruilei Optoelectronics Technology Co., Ltd, China) at different power intensity (1, 2 or 3 W/cm²) at different concentrations (25, 50, 100, 200 µg/mL of ZnPc) for 10 min. The thermal profiles of ZnPc, DLQ/ZnPc, DLQ/DOX and DLQ/DZ were investigated using 808 nm laser irradiation (2 W/cm² for 10 min) with 200 µg/mL of ZnPc.

In vitro click efficiency and cellular uptake

To evaluate click efficiency, MCF-7 breast cancer cells were incubated in confocal dish at 3×10⁴ cells/dish for 24 h. Following this, MCF-7 cells were treated with 50 µM Ac4ManNAz or serum-free medium for 3 days, respectively. Afterwards, MCF-7 cells were incubated with 20 µM DBCO-Cy5 for 2 h, observed using confocal laser scanning microscopy (LSM700, Carl Zeiss), and analyzed using flow cytometry (BD Accuri C6, USA). Furthermore, MCF-7 cells were seeded in confocal dishes at 3×10⁴ cells/dish and left to grow for 24 h. Afterwards, MCF-7 cells were treated with 50 µM Ac4ManNAz or serum-free medium for 3 days, respectively. Cultured in serum-free medium cells were treated with DLQ-Cy5 medium solution and used as control. The other cells were prepared *via* replacing Ac4ManNAz medium with DBCO-Cy5 or DLQ-Cy5 medium solutions. Afterwards, the cells cultured for 0.5, 1, 2 or 4 h. To visualize cell nuclei, each dish was washed 3 times with PBS and mixed with Hoechst 33342 for 20 min. Following this, the cells were fixed with 4% paraformaldehyde solution for 20 min and observed using the confocal laser scanning microscopy.

To assess cellular uptake, MCF-7 cells were seeded in confocal dishes at 3×10⁴ cells/dish and left to grow for 24 h. Afterwards, the MCF-7 cells were treated with 50 µM Ac4ManNAz or serum-free medium for 3 days, respectively. Following this, DOX, ZnPc, or DLQ/DZ solutions were added to the cells cultured in serum-free medium and left to grow for 6 h and 24 h, respectively. A+DLQ/DZ group was

prepared by replacing Ac4ManNAz medium with DLQ/DZ medium for 6 h and 24 h. Additionally, tris (2-carboxyethyl)-phosphine (TCEP) was added for 10 min before adding DLQ/DZ as competitive inhibition group. To visualize cell nuclei, each dish was washed 3 times with PBS and mixed with Hoechst 33342 for 20 min. Afterwards, the cells were fixed with 4% paraformaldehyde solution for 20 min and observed using the confocal laser scanning microscopy (Leica TCS SP5, Germany).

In vivo imaging study

Dynamic distribution of DLQ-Cy5 and DLQ/DZ nanocomposites *in vivo* was monitored using real time imaging. To model MCF-7 breast tumor-bearing nude mice, MCF-7 cell suspension (200 μ L; 1×10^7 cells/mL) was subcutaneously injected into the female nude mice. The mice, bearing expected tumor volume (~ 500 mm³), were randomly divided into 6 groups (3 mice/group): free Cy5, A+DBCO-Cy5, A+DLQ-Cy5, DLQ/DZ, A+DLQ/DZ, and A+TCEP+DLQ/DZ. The A-containing groups were injected intratumorally with Ac4ManNAz (40 mg/kg) once a day for three days. Following this, the mice were administered with Cy5, DBCO-Cy5, DLQ-Cy5 or DLQ/DZ using intravenous injections, respectively. The Cy5 dose was 300 μ g/kg. The ZnPc dose was 2 mg/kg. To quench azide groups, competitive inhibition group was intravenously injected with a large amount of TCEP (10 mM) and kept for 1 h. Afterwards, DLQ/DZ solution was injected intravenously. Fluorescence images were observed and photographed at 2, 4, 8, 12, and 24 h after administration. The tumor-bearing nude mice were euthanized after 24 h of administration. All major organs (including heart, liver, spleen, lung, kidney) and tumor tissues were dissected. Finally, each tissue fluorescence image was photographed and semi-quantitatively analyzed. All experiments with animals were approved by the Institutional Animal Care and Use Committee of China Pharmaceutical University.

In vivo temperature measurement

The photothermal conversion capability of DLQ/DZ nanocomposites was investigated in MCF-7 tumor-bearing nude mice using infrared thermal camera (E5, FLIR). The tumor-bearing mice (tumor volume ~ 200 mm³) were randomly divided into 3 groups (3 mice/group): saline, DLQ/DZ, and A+DLQ/DZ. Mice in A+DLQ/DZ group were injected intratumorally with Ac4ManNAz (40 mg/kg) once a day for three days. Afterwards, saline or DLQ/DZ (5 mg ZnPc/kg) were injected intravenously and left for 24 h. To anesthetize, mice were intraperitoneally injected with chloral hydrate (2

mg/kg). Afterwards, the tumor sites of tumor-bearing mice were irradiated at 2 W/cm² for 5 min. The thermographic images were determined using infrared thermal camera.

In vitro cytotoxicity

To determine the cell cytotoxicity of DLQ/DZ nanocomposites, methyl thiazolyl tetrazolium (MTT, 3-(4,5-dimethylthiazol-2-yl)-2,5-diphenyltetrazolium bromide) assay was performed. MCF-7 cells were seeded in 96-well plates at 5000 cells/well, kept for 24 h, and divided into 11 groups: 1. ZnPc; 2. ZnPc+Laser; 3. DOX; 4. DOX+ZnPc+Laser; 5. DLQ/ZnPc; 6. DLQ/ZnPc+Laser; 7. DLQ/DOX; 8. DLQ/DZ+Laser; 9. A+DLQ/DZ+Laser; 10. DLQ; and 11. Ac4ManNAz. The A-containing groups were pre-incubated with Ac4ManNAz (50 μ M) for 3 days. Afterwards, cells were incubated with different formulations. Following 4 h-incubation, laser group cells were irradiated for 5 min using 808 nm laser (2 W/cm²). Following 24 h-incubation, all cells were added 40 μ L MTT (2.5 mg/mL) and left for 4 h. Afterwards, 150 μ L DMSO was used to replace medium and dissolve formazan crystals. Absorbance was detected using a microplate reader (POLARstar Omega, BMG LABTECH) at 490 nm. The cell viability was calculated according to the following formula:

$$\text{Cell viability (\%)} = \frac{(A_{\text{test}} - A_{\text{blank}})}{(A_{\text{control}} - A_{\text{blank}})} \times 100\%$$

A_{test} , A_{control} , and A_{blank} indicate measured absorbances for test (with formulation added), control (without formulations), and blank (without cells and formulations) groups, respectively.

In vivo anti-tumor efficacy test

Tumor-bearing mice (tumor volume ~ 50 mm³) were randomly divided into 6 groups (5 mice/group): 1. Saline; 2. DOX; 3. DLQ/DOX; 4. DLQ/ZnPc; 5. DLQ/DZ; and 6. A+DLQ/DZ. The A-containing group was injected intratumorally with Ac4ManNAz (40 mg/kg) once a day for three days. The doses of DOX and ZnPc were 5 mg/kg. The formulations were administered using tail vein injection on days 0, 3, and 6. The 4, 5 and 6 groups were irradiated with 808 nm near-infrared light for 5 min (2 W/cm²) at days 1, 4, and 7. Tumor volumes were measured daily and calculated using the following formula: (A indicates the tumor width and B indicates the tumor length).

$$V = (A^2 \times B) / 2$$

Mice were euthanized on day 20 after injections. Extracted organs (heart, liver, spleen, lung, kidney) and tumors were fixed in 10% (v/v) formalin for immunohistochemistry analysis. Afterwards, the tumor tissues were washed and embedded in

paraffin. Sectioned and mounted on slide tissues were stained using H&E and Ki67 immunohistochemical protocols. Slides were observed under an inverted microscope and photographed. The tumor inhibition rate (IR) was calculated according to the following formula: (W_{saline} indicates the average tumor weight of the saline group and W_{sample} indicates the average tumor weight of the formulation groups).

$$\text{IR (\%)} = (W_{\text{saline}} - W_{\text{sample}}) / W_{\text{saline}} \times 100\%$$

Evaluations of potential side effects associated with drug administration

The body weight of each tumor-bearing mice was recorded daily. Body weight changes were evaluated for signs of systemic toxicity. Additionally, AST (aspartate transaminase), ALT (alanine aminotransferase), and CK (creatin kinase) values in serum of tumor-bearing mice were measured to assess liver and heart toxicity after 20 day-treatment.

Statistical analysis

Data were given as mean \pm standard deviation (SD). Statistical significance was analyzed by one-way unweighted mean analysis of variance (ANOVA) and statistical significance was set at $P < 0.05$.

Results and Discussion

Synthesis and characterization of DLQ conjugate

In this study, the amphiphilic DLQ conjugates were synthesized by a two-step reaction as shown in Figure S8. LMWH, a substance with many carboxyl groups [44], was conjugated with DBCO and Qu by acylation or esterification reactions, respectively. The chemical structure of DLQ conjugates (shown in yellow color, Figure S9) was verified using $^1\text{H-NMR}$ and FT-IR. In the $^1\text{H-NMR}$ spectra (Figure S10), the characteristic peak of LMWH was detected at 5.1 ppm and the peaks of DBCO appeared at 1.8 ppm, 5.2 ppm and 7.0-8.0 ppm in the DL spectra. The shown peaks of 8.2 and 6.0-7.0 ppm belonged to Qu, suggesting the formation of DLQ conjugates. In the FT-IR spectra of LMWH (Figure S11), the absorption peaks at 3468.6 cm^{-1} and 1627.6 cm^{-1} were attributed to hydroxyl and carbonyl stretching vibrations of LMWH, respectively. Compared to LMWH spectra, the new absorption bands at 1682.8 cm^{-1} and 1563.0 cm^{-1} were ascribed to I (C=O stretching vibration) and II (N-H bending vibration) bands of amide bond in DL spectra, respectively, indicating that LMWH and DBCO was conjugated by amide bonds. Furthermore, characteristic absorption bands of ester bonds (1730.6 cm^{-1}) and amide bonds (1684.2 cm^{-1} and 1567.7 cm^{-1}) were observed in DLQ spectra, confirming the

successful synthesis of DLQ conjugates. The molar grafting ratios of DBCO and Qu in DLQ conjugates were 29.8% and 15.0%, respectively (Figure S12). The critical aggregation concentration (CAC) of the DLQ was $77.76\text{ }\mu\text{g/mL}$ (Figure S13), indicating that DLQ conjugation would self-assemble into nano-sized system at a low concentration and possess excellent dilution stability [45].

Preparation and characterization of DLQ/DZ nanocomposites

The DBCO-modified, co-incorporating DOX and ZnPc (DLQ/DZ) nanocomposites were prepared using dialysis method (Figure 1A). Two single drug loaded nanocomposites (i.e. DLQ/DOX and DLQ/ZnPc) were also prepared as controls. As shown in Figure 1B, 1C and 1D, the particle size of dual-loading DLQ/DZ nanocomposites was $198.2\pm 2.4\text{ nm}$ (shown in dark blue color with a spherical shape in Figure S14). Other control nanocomposites demonstrated similar particle size distributions (shown in different colors). The nano-scaled particle of this size demonstrated unique tumor tissue-specific permeability and retention [46]. Additionally, these formulations were negatively charged ($> 20\text{ mV}$), able to avoid plasma protein adsorption to a great extent, and prolong time of nanocomposites circulation in blood [47, 48].

Surprisingly, DOX- and ZnPc-loading levels in DLQ/DZ nanocomposites were approximately 10%, i.e. up to about 20% of total drug loading was achieved; while the drug loadings in DLQ/DOX and DLQ/ZnPc nanocomposites were $10.6\pm 3.2\%$ and $11.2\pm 2.1\%$ respectively. It was indicated that drug co-loading increased total drug loading capacity of DLQ nanocomposites, which made DLQ/DZ nanocomposites an optimal nanosystem for combination therapy. The joint effect of hydrophobic and π - π stacking interactions among DOX, ZnPc and Qu might be the driving force of elevated drug loading. This also appeared to have improved the stability of nano-system as shown in Figure 1E. The particle sizes of DLQ/DOX nanocomposites remained relatively stable in water only within 48 h; while no significant size changes were observed for DLQ/DZ and DLQ/ZnPc nanocomposites during over 120 h.

Furthermore, the *in vitro* release behavior of DOX from nanocomposites was evaluated in PBS buffer at pH 7.4, 5.8 and 4.5. As shown in Figure 1F, the cumulative amount of released DOX was lower at pH 7.4 compared to pH 5.8 and 4.5. The effects might be associated with destruction of electrostatic interactions between drug molecules and DLQ under the acid pH conditions [15, 49, 50]. The observed

drug-release property favored the agent therapeutic effect in the acidic microenvironment of tumors.

The photo-thermal conversion capability of DLQ/DZ nanocomposites

Previous studies demonstrated that temperature above 48 °C effectively kills tumor cells [51], *i.e.* the temperature increments (ΔT) > 18 °C (*via* the subcutaneous tumor temperature of ~30 °C) were believed to induce necrosis in tumor cells. The photo-thermal conversion capability of DLQ/DZ nanocomposites was investigated using laser irradiation. As shown in Figure 1G, the temperature of DLQ/DZ solution was gradually increased along with the increases in irradiation time and power

density. We found that the ΔT of DLQ/DZ solution irradiated at 2 W/cm² and 3 W/cm² rapidly went up to 20.5 °C and 28.7 °C during 60 s, respectively. These results revealed the favorable potential of laser power to kill tumor cells at 2 W/cm² or 3 W/cm². Additionally, irradiating at 2 W/cm² in DLQ/DZ solution (concentration range of 25-200 µg/mL) for 600 s forced ΔT to rise from 29.3 to 42.8 °C (Figure 1H); while using distilled water (as control) resulted in negligible temperature changes (< 5 °C) under equal conditions. These results indicated that the thermal effect induced by DLQ/DZ nanocomposites strongly depended on power density and ZnPc concentration. It was noted that the ability of DLQ/DZ and DLQ/ZnPc nanocomposites to convert photo energy

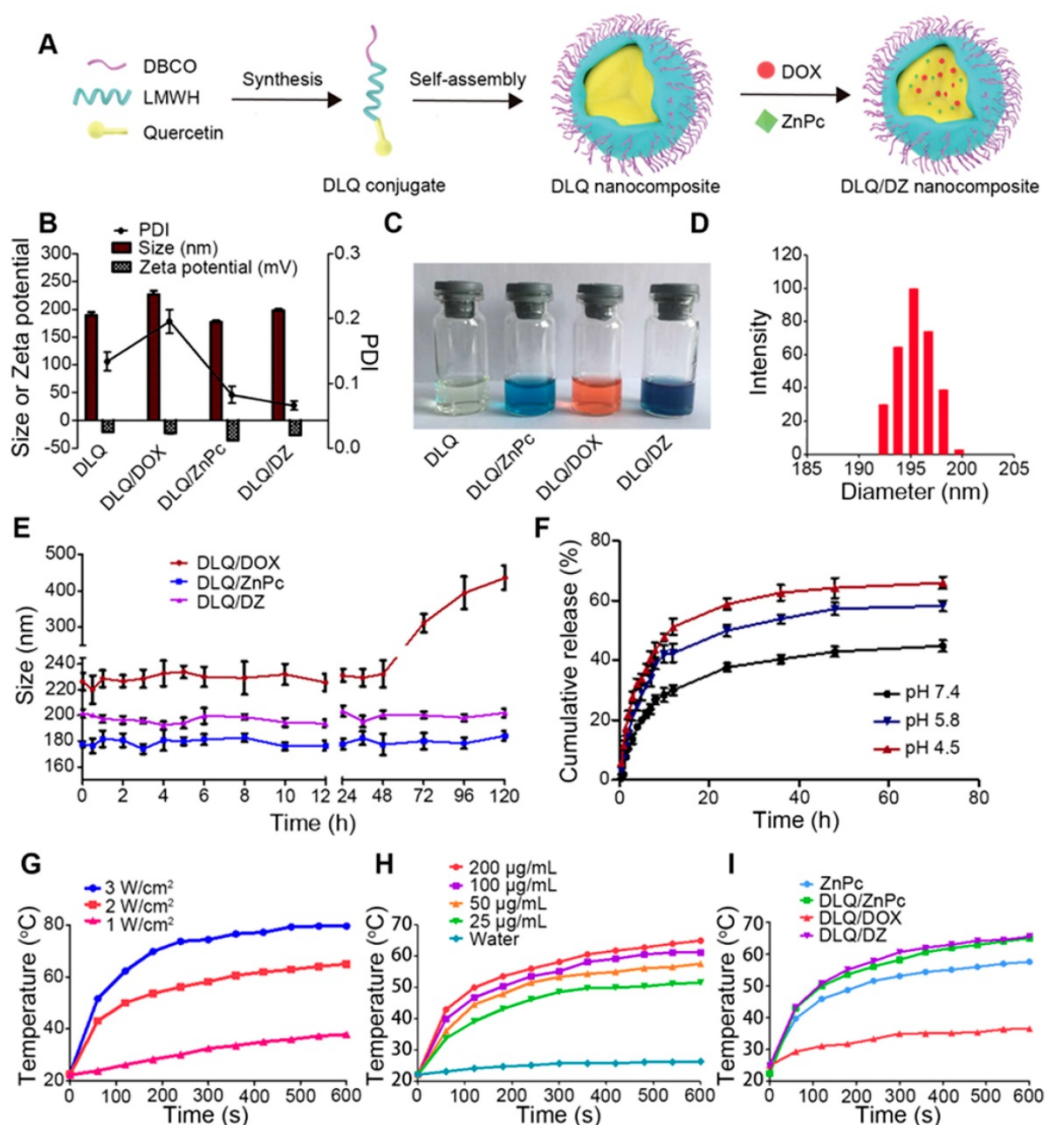


Figure 1. (A) Synthesis and assembly process of DLQ/DZ nanocomposites. (B) The polydispersity index (PDI), particle size and zeta potential of DLQ, DLQ/DOX, DLQ/ZnPc, and DLQ/DZ nanocomposites. (C) Photographs of DLQ, DLQ/ZnPc, DLQ/DOX, and DLQ/DZ nanocomposites in distilled water. (D) The DLS image of DLQ/DZ nanocomposites. (E) The stability of DLQ/DOX, DLQ/ZnPc, and DLQ/DZ nanocomposites in distilled water for 120 h. (F) *In vitro* release of DOX from DLQ/DZ nanocomposites at pH 7.4, pH 5.8 and pH 4.5 at 37 °C. (G) The temperature elevation profiles of DLQ/DZ nanocomposites in different laser power (1, 2 and 3 W/cm²) for 600 s. (H) The temperature elevation profiles of DLQ/DZ nanocomposites at different ZnPc concentration (25, 50, 100 and 200 µg/mL). (I) The temperature elevation profiles of ZnPc, DLQ/ZnPc, DLQ/DOX, and DLQ/DZ upon 808 nm laser irradiation at 2 W/cm².

into thermal energy was much higher than the ability of free ZnPc solution (Figure 1I), indicating that the encapsulation of ZnPc into DLQ nanocomposites favored their photothermal conversion. Consequently, the photothermal profiles of DLQ/DZ and DLQ/ZnPc nanocomposites were similar during the irradiation; while the DLQ/DOX solution showed only a slight temperature elevation due to light exposure. Furthermore, the photothermal conversion efficiency of DLQ/DZ nanocomposites exposed to 808 nm continuous laser was 21.9% (Figure S15-S16). The photothermal performance remained stable after four

irradiation natural cooling cycles (Figure S17). In brief, DLQ/DZ nanocomposites possessed high photothermal conversion efficiency, which could favor photothermal therapy *in vivo*.

Generation of azide groups and *in vitro* click reaction efficiency

The tumor cells and nanocomposites click efficiency is a key component of tumor-targeted therapy [36]. In this case, it was essential that metabolic precursor (Ac4ManNAz) firstly produced abundant non-natural azide groups on the surface of MCF-7 tumor cells through intracellular metabolic

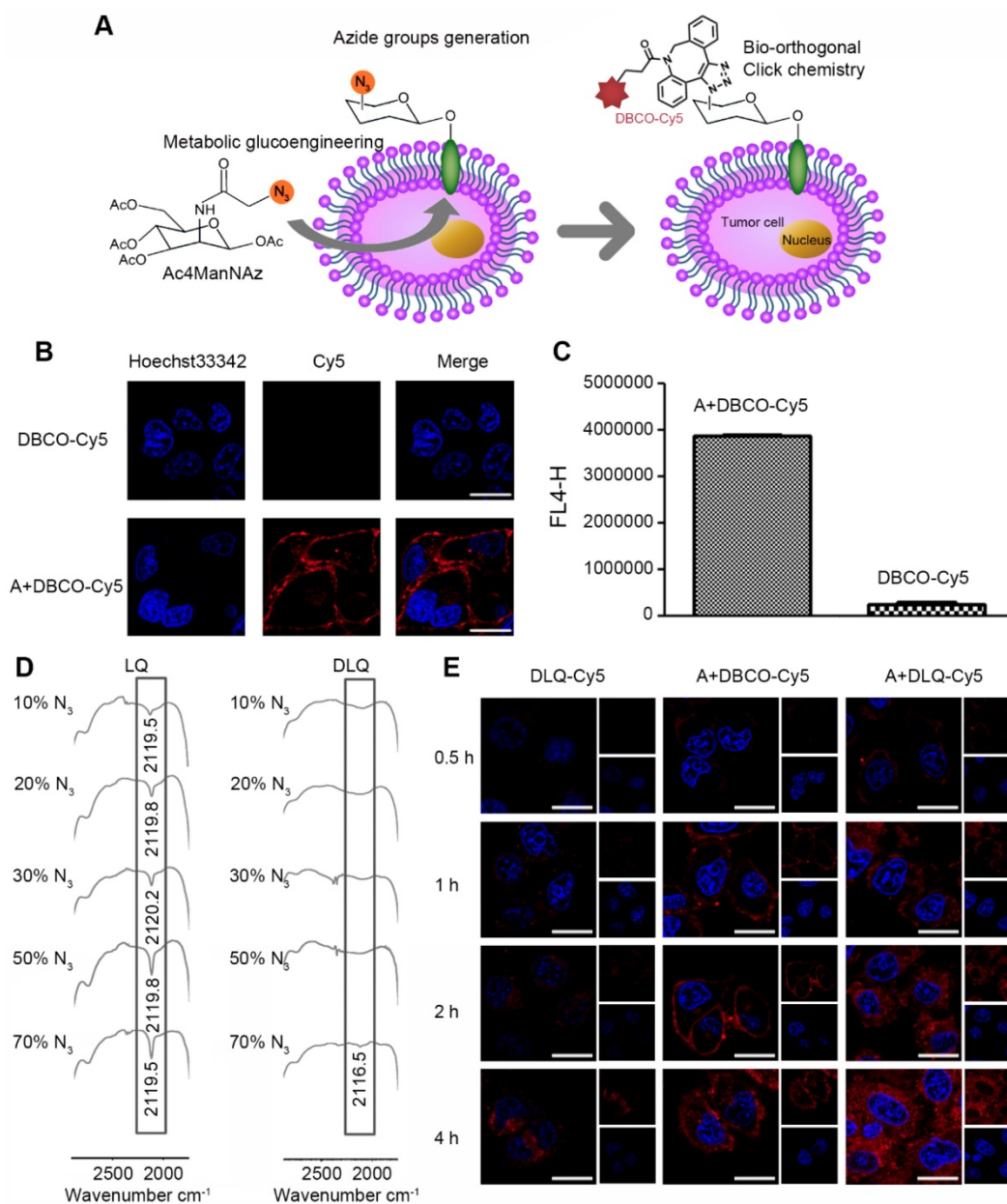


Figure 2. (A) Schematic illustration of tumor cell-targeting strategy by metabolic glucoengineering and bio-orthogonal click chemistry. (B) Visualization of azide groups (red) on the surface of Ac4ManNAz-treated MCF-7 cells, and the cells without Ac4ManNAz-treated were used as a control. Scale bar is 20 μm for all images. (C) Mean fluorescence intensity detected by flow cytometry in MCF-7 cells after incubation with DBCO-Cy5 for 2 h. (A: Ac4ManNAz pre-treated MCF-7 cells). (D) FT-IR spectra of LQ or DLQ nanocomposites with different percentages of azide groups (10%, 20%, 30%, 50% and 70%). (E) Cellular binding and uptake for 0.5 h, 1 h, 2 h and 4 h after incubation with DLQ-Cy5, A+DBCO-Cy5, A+DLQ-Cy5. Scale bar is 20 μm.

glycoengineering [35]. To detect the azide groups on the membrane of tumor cells, DBCO-Cy5 was chosen because it could specifically bound to the azide groups *via* bio-orthogonal copper-free click chemistry reaction [33] and could be directly visualized by the spontaneous red fluorescence (Figure 2A). The number of azide groups on the surface of tumor cells was calculated to be 3.23×10^7 /cell through determining the fluorescence intensity of the MCF-7 cells pretreated with Ac4ManNAz after incubation with DBCO-Cy5 for 1 h (Figure S18). The intensity was significantly higher than that of naturally expressed receptors (e.g. laminin-binding intensity (10^3 - 10^5 /cell) reported in previous studies [37, 52]). In other words, the number of the targetable receptors was enhanced by 2-4 orders of magnitude in our case. The large number of azide groups produced on cell membranes provided more opportunities and higher probability for subsequent initiation of cell-level click chemistry reactions.

Furthermore, click reaction efficiency of DBCO and azide groups was investigated by confocal imaging, flow cytometry, and FT-IR analysis *in vitro*. As shown in Figure 2B, the A+DBCO-Cy5 group generated strong red fluorescence signal at MCF-7 cell membranes after incubation for 2 h; while the DBCO-Cy5 group without pretreatment with Ac4ManNAz showed no obvious red fluorescence. The quantitative analysis demonstrated that the fluorescence intensity of the A+DBCO-Cy5 group was significantly higher than that of the DBCO-Cy5 group (almost 9 times) (Figure 2C). The observed increase was attributed to the effective generation of azide groups on the surface of MCF-7 cells. The excellent click reaction efficiency of DBCO and azide groups on the surface of tumor cells demonstrated successful combination of metabolic glycoengineering with bio-orthogonal copper-free click chemistry, which may lead to high potential in tumor-targeted drug delivery.

The click chemistry reaction efficiency of the DLQ nanocomposites and azide groups was measured using the absorption peak of azide groups (around 2100 cm^{-1}) within FT-IR spectrum 2 h after initiation of the reaction. The LQ nanocomposites without DBCO was used as the control. As shown in Figure 2D, in the LQ group, along with the increasing quantity of azide groups incubated, the azide group absorption peak became sharper. On the contrary, when 10%-50% of azide groups were exposed to DLQ, the absorption peak completely disappeared, indicating that all azide groups completely reacted with DLQ nanocomposites in water. However, some of the azide groups did not react when their amount reached 70% (represented by a tiny peak, Figure 2D).

Meanwhile, when 50% azide groups were exposed to the DLQ in serum or tumor homogenate, the azide groups completely reacted with DLQ nanocomposites (Figure S19). These results indicated that at least 50% of azide groups were specifically clicked to DBCO on the DLQ within 2 h, suggesting that the click chemistry reaction was fast and highly efficient *in vitro* and *in vivo*.

The intracellular fate of DBCO-based nanocomposites was monitored by grafting of the fluorescent dye Cy5 into the DLQ conjugates. Subsequently, we investigated the time course of click reaction on the surface of MCF-7 cells and associated intracellular processing of DLQ-Cy5 nanocomposites using confocal laser scanning microscopy. As shown in Figure 2E, the fluorescence intensity in all experimental groups gradually increased over time, suggesting that the cellular uptake was time-dependent. Analyzing time-lapse imaging, we found that DBCO-Cy5 fluorescence in Ac4ManNAz-pretreated cells mainly appeared on the cell membranes at different time points. The data indicated the occurrence of click reactions based on DBCO and azide groups on tumor cell membranes. However, low level of fluorescence was detected in the cytoplasm during 4 h of A+DBCO-Cy5 treatment. The red fluorescence of DLQ-Cy5 in Ac4ManNAz-pretreated cells was observed on the cell membrane as early as 0.5 h, and was then successively taken up into the cells since 1 h. These results suggested that DLQ-Cy5 nanocomposites were first bound to the tumor cells by click chemical reactions and then entered into the cells *via* endogenous glycan internalization and endocytosis [33]. Furthermore, the cell cytoplasm in the A+DLQ-Cy5 group was marked by strong red fluorescent signal at 4 h. The effects were also significantly higher than that in the DLQ-Cy5 group, revealing the effective and fast tumor cellular uptake was mainly based on specific reactions between the DBCO on DLQ nanocomposites and the azide groups on the surface of tumor cells. Interestingly, DLQ-Cy5 nanocomposites exhibited significantly different intracellular distribution and efficiency compared with DBCO-Cy5, which was attributed to the polyvalent interactions [53-55] of nanocomposites. In other words, multiple DBCO on the nanocomposites can simultaneously bind to multiple azide groups on the cell surface compared to the monovalent interaction of single molecules. Thus, the superiority of DBCO-based nanocomposites can be used to improve tumor-targeted drug delivery. Taken together, DLQ nanocomposites with the capacity of efficient clicking with the azide groups generated by tumor cells offered the prerequisite for effective drugs uptake by tumor cells.

Cellular uptake and biodistribution of DLQ/DZ nanocomposites

To validate the efficient and prominent tumor-targeting ability of DBCO-modified nanocomposites, we investigated the nanocomposites cell-uptake *in vitro* and biodistribution of DLQ/DZ nanocomposites *in vivo* using confocal laser scanning microscopy and non-invasive optical imaging system, respectively. As shown in Figure 3A, the red (DOX) and green (ZnPc) fluorescence intensities in A+DLQ/DZ group were notably higher than those in the DLQ/DZ group, suggesting that bio-orthogonal click reactions on the surface of tumor cells effectively increased the cellular uptake of DLQ/DZ nanocomposites. This was also supported by the results observed in the A+TCEP+DLQ/DZ group. The fluorescence signals of DOX and ZnPc were dramatically weakened after treatment with azide-quenching agent TCEP. The red fluorescence of DOX in the A+DLQ/DZ group was observed in the cytoplasm and cell membrane at 6 h; while there was

no significant fluorescent signal on the cell membrane in the DLQ/DZ group without pre-treatment with Ac4ManNAz, further supporting that the cellular uptake of DLQ/DZ nanocomposites relied on binding to azide groups on the cell surface. Notably, the green fluorescence of ZnPc in the A+DLQ/DZ group was localized in the cytoplasm rather than retained at the cell surface at 6 h, which could be associated with the self-quenching effect of ZnPc encapsulated in nanocomposites [56, 57]. The quenched ZnPc fluorescent signals were recovered once the encapsulated ZnPc was released after cell internalization contributing to stronger green fluorescent signals in cytoplasm. After incubation of the Ac4ManNAz-pretreated MCF-7 cells with DLQ/DZ for 24 h, DOX was mostly observed in the cell nuclei; while ZnPc was homogeneous distributed in the cytoplasm. The suitable intracellular distribution would help chemotherapy drug and photothermal conversion agent to achieve better therapeutic effects.

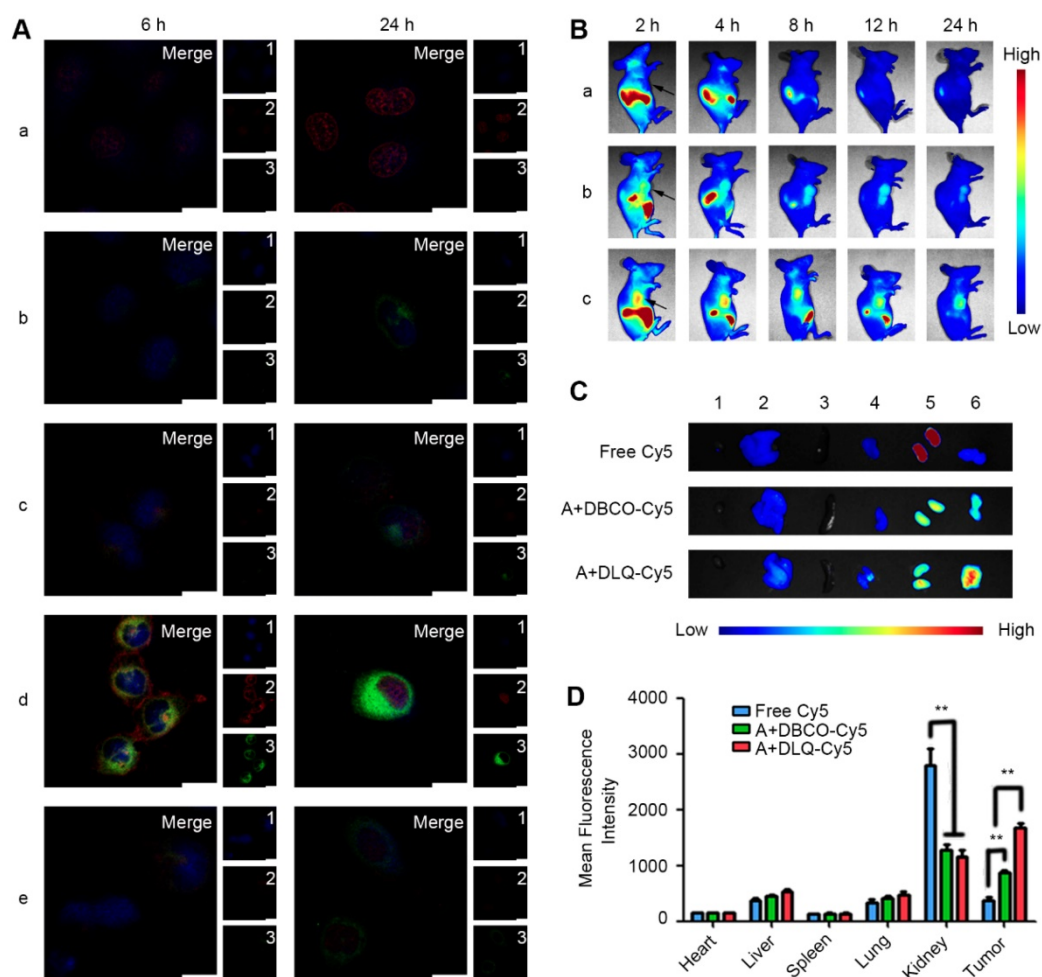


Figure 3. (A) Time-dependent cellular uptake after 6 h and 24 h incubation with DOX (a), ZnPc (b), DLQ/DZ (c), A+DLQ/DZ (d), and A+TCEP+DLQ/DZ (e) in MCF-7 cells. 1: Nucleus (blue); 2: DOX (red); 3: ZnPc (green); Merge: overlay of 1, 2 and 3. Scale bar is 20 μ m. (B) *In vivo* NIR fluorescence images of MCF-7 tumor-bearing nude mice at 2 h, 4 h, 8 h, 12 h, and 24 h following injection free Cy5 (a), A+DBCO-Cy5 (b) and A+DLQ-Cy5 (c). Arrows indicated the tumor site. (C) *Ex vivo* NIR fluorescence images of hearts (1), livers (2), spleens (3), lungs (4), kidneys (5), and tumors (6) at 24 h post-injection. (D) Quantitative analysis of mean fluorescence intensity in normal tissues and tumors at 24 h post-injection. Data are represented as mean \pm SD (n=3). **P < 0.01.

Non-invasive optical imaging was used to track the *in vivo* distribution of DLQ nanocomposites (labeled covalently with Cy5). As shown in Figure 3B and 3C, the A+DLQ-Cy5 group was marked by stronger and longer-lasting in-tumor fluorescence compared to that in the A+DBCO-Cy5 and free Cy5 groups. The in-tumor fluorescent intensity was 1.9-times and 4.6-times higher than that in the A+DBCO-Cy5 and free Cy5 groups, respectively. Moreover, obviously decreased distribution of the dye in kidneys was obtained in two other groups compared with free Cy5 group ($P < 0.01$) (Figure 3D). These results indicated the important role of DBCO-mediated bio-orthogonal click reaction in improving their biodistribution *in vivo*. Such distribution could also reduce potential adverse effects. Meanwhile, tumor-targeting nanocomposites (A+DLQ-Cy5) were preferable materials for anti-tumor drug delivery compared to small molecules (A+DBCO-Cy5) [53-55].

Besides the selective accumulation of nanocarriers at tumor tissues, opportune drug-release from nanocarriers is of equal importance for anticancer drugs in tumor cells, which is the ultimate goal of effective anti-tumor drug delivery. To study the drug delivery efficiency of DLQ nanocomposites, we further investigated the biodistribution of drugs using fluorescence signals emitted by ZnPc (encapsulated in the DLQ/DZ nanocomposites). As shown in Figure 4, *in vivo* and *ex vivo* tumor fluorescence signals in the A+DLQ/DZ group were higher than those in the DLQ/DZ group. The result was consistent with the *in vitro* results of the cellular uptake experiments (Figure 3A). When the azide groups on the surface of tumor cells were quenched by TCEP as an inhibitor (A+TCEP+DLQ/DZ group), the fluorescence signal within tumor tissues decreased significantly. This illustrated that the generation of azide groups on the surface of the tumor cells was a prerequisite for the bio-orthogonal click chemistry to prompt accumulation of DLQ/DZ nanocomposites at tumor sites *in vivo*. Considering the relatively short residence of empty nanocarriers in tumors (about 12 h, as shown in Figure 3B), we found weak ZnPc fluorescence signals at 2 h, which kept increasing until 24 h (Figure 4A). These results indicated that the drugs were efficiently delivered by DLQ vectors, released into tumor cells, and recovered fluorescence signals. The fluorescence was maintained in tumor for more than 24 h, suggesting a favorable drug accumulation and retention in tumor cells, which was supposed to facilitate the anti-tumor effect of drugs. Furthermore, the level of in-tumor

ZnPc in the A+DLQ/DZ group was significantly higher than that in other tissues including liver and spleen (Figure 4B and 4C) and corresponded to the distribution efficiency of empty DLQ carriers *in vivo* (Figure 3D). Comparing the traditional tumor-targeting nanoparticles, including our previous studies [40, 58], the distribution of nanoparticles or drugs in tumor tissue was similar or lower than that in the liver or spleen. Thus, highly selective tumor-targeting achieved in the current study illustrated the superiority and promising prospect of elaborated artificial modification strategy in tumor targeting nanocomposite designation.

***In vitro* cytotoxicity and *in vivo* photothermal conversion**

MTT assay and *in vivo* infrared thermography were utilized to assess the effect of the enhanced tumor-targeting delivery on cytotoxicity and photothermal conversion, respectively. The viability of cells treated with Ac4ManNAz and DLQ nanocomposites was above 90% (Figure S20), suggesting their minor cytotoxicity against MCF-7 tumor cells. Additionally, the difference in cell viability between the laser-exposed (ZnPc+Laser and DLQ/ZnPc+Laser) and non-exposed (ZnPc and DLQ/ZnPc) groups indicated that ZnPc had higher NIR cytotoxicity (Figure 5A). Moreover, DOX+ZnPc+Laser group exhibited remarkably enhanced cytotoxic response than that in the DOX or ZnPc+Laser groups alone. Similarly, the cell mortality in the DLQ/DZ+Laser group was significantly higher than that in the DLQ/DOX and DLQ/ZnPc+Laser groups (Figure 5B). Furthermore, the calculated combination index (CI) values of DOX+ZnPc+Laser and DLQ/DZ+Laser using the half maximal inhibitory concentration of agents in MCF-7 cells were 0.6, suggesting a synergistic effect of chemotherapy and PTT. Importantly, a sharp decrease in cell viability was found in the A+DLQ/DZ+Laser group compared to the DLQ/DZ+Laser group. It suggested that the combined strategy of metabolic glycoengineering and click chemistry improved the cytotoxicity of DLQ/DZ nanocomposites.

The infrared thermography results shown that the A+DLQ/DZ treatment promoted the tumor surface temperature in mice *via* increased tumor accumulation of PTT agents. As shown in Figure 5C, laser irradiation (808 nm at 2 W/cm²) for 5 min increased the tumor surface temperature in mice in the A+DLQ/DZ-treated group to 57 °C; while in DLQ/DZ-treated group, temperature was increased to 51 °C under the same condition.

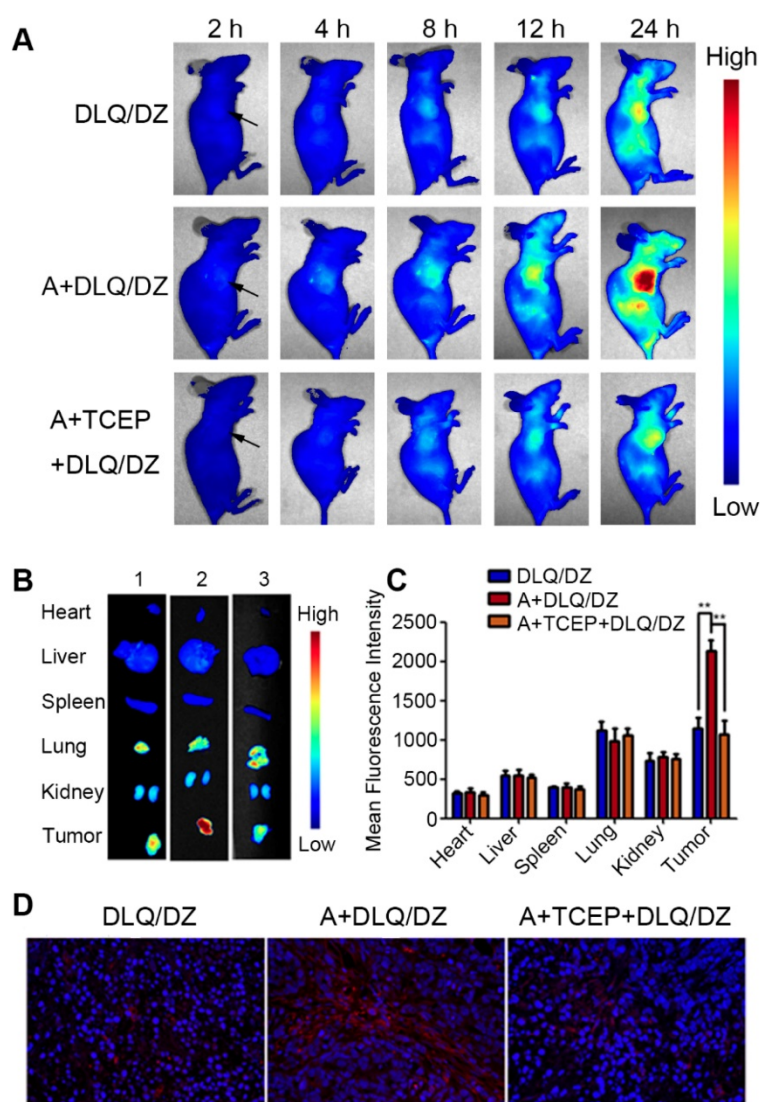


Figure 4. (A) *In vivo* fluorescence images of MCF-7 tumor-bearing nude mice at 2 h, 4 h, 8 h, 12 h and 24 h following injection DLQ/DZ, A+DLQ/DZ and A+TCEP+DLQ/DZ. Arrows indicate the tumor site. (B) *Ex vivo* fluorescence images of heart, liver, spleen, lung, kidneys and tumor at 24 h post-injection of DLQ/DZ (1), A+DLQ/DZ (2), A+TCEP+DLQ/DZ (3). (C) Quantitative analysis of mean fluorescence intensity in normal tissues and tumors. Data are represented as mean \pm SD (n=3). **P < 0.01. (D) Fluorescence images (400-fold magnification) of tumor sections. Red was ZnPc and blue (DAPI) was the nucleus.

In vivo anticancer efficacy

Encouraged by the bio-distribution and infrared thermal imaging data *in vivo*, we further evaluated the therapeutic potential of DLQ/DZ nanocomposites on MCF-7 human tumor-bearing nude mice. As shown in Figure 6A, the data could be divided into three categories. Firstly, single agent treated groups such as DOX, DLQ/DOX or DLQ/ZnPc groups demonstrated a moderate inhibition of tumor growth (less desirable in cancer therapy). Secondly, in the DLQ/DZ groups, two-component simultaneous delivery of DOX and ZnPc exhibited stronger antitumor effect compared to single agent treated groups ($P < 0.01$), implying that the two-component combination of chemotherapy and PTT was more effective than monotherapy. However, DLQ/DZ

treatment did not completely suppress tumor growth, likely due to insufficient accumulation of nanocomposites in tumor site. Excitingly, the tumor growth of mice after three-component combined treatment (in the A+DLQ/DZ group) was well controlled by the aid of efficient and specific tumor targeting delivery, and the tumor-inhibition rate was up to 96.1%. The effect was better than those observed in the two-component treatment (DLQ/DZ: 83.3%) and the single treatment (DOX: 51.5%, DLQ/DOX: 63.7%, DLQ/ZnPc: 72.7%) groups. Furthermore, it was worth noting that the tumor volume in mice from the A+DLQ/DZ group was not increased during the investigated period, even after the schedule of the drug administration and irradiation (9-20 days) compared to other groups, indicating an excellent and long-lasting inhibition of tumor progression. The

tumor weight and appearance (Figure 6B and 6C) also demonstrated a desirable mutually synergistic performance of the therapy in the A+DLQ/DZ group. Immunohistochemistry analysis exhibited larger necrosis area (84.7%) and lower proliferation index (11.3%) in the A+DLQ/DZ group (Figure 6D, 6E, and 6F). These results indicated that A+DLQ/DZ group yielded the highly efficient antitumor effect. The effect was supported by the fast and tumor-specific drug delivery of DLQ/DZ nanocomposites using the bio-orthogonal click-targeting that intensified accumulation of both drugs in tumor cells. The accumulation led to the rapid rise of temperature in tumor tissues (Figure 5C) and contributed to more effective tumor ablation allied with chemotherapeutics (Figure 6A). Meanwhile, the achieved hyperthermia further facilitated the deep tumor penetration of chemotherapeutics by expanding endothelial gaps and enhancing blood pressure and blood flow [18-21], and increased the

tumor drug accumulation *via* enhancing vascular permeabilization [22], forming a positive feedback loop.

In vivo potential side effects of nanocomposites

The Figure 6C was the visual therapeutic results in tumor-bearing nude mice after 9 and 20 days of treatment. The A+DLQ/DZ group showed obvious photothermal damage and scar formation at the tumor site on day 9 post-treatment. The scar tissue was shed at day 20 confirming good *in vivo* tolerance to the A+DLQ/DZ nanocomposites. The body weight (Figure 7A) of tumor-bearing nude mice in DOX group decreased significantly on day 9. The ALT value (Figure 7B) increased significantly in this group compared to saline group, indicating that DOX had severe systemic and hepatotoxic effects. In contrast, DLQ/DOX group showed an increase in body weight and a decrease in ALT value ($P < 0.05$) compared to DOX group, suggesting that DOX encapsulation in nanocomposites could reduce its toxicity. Moreover,

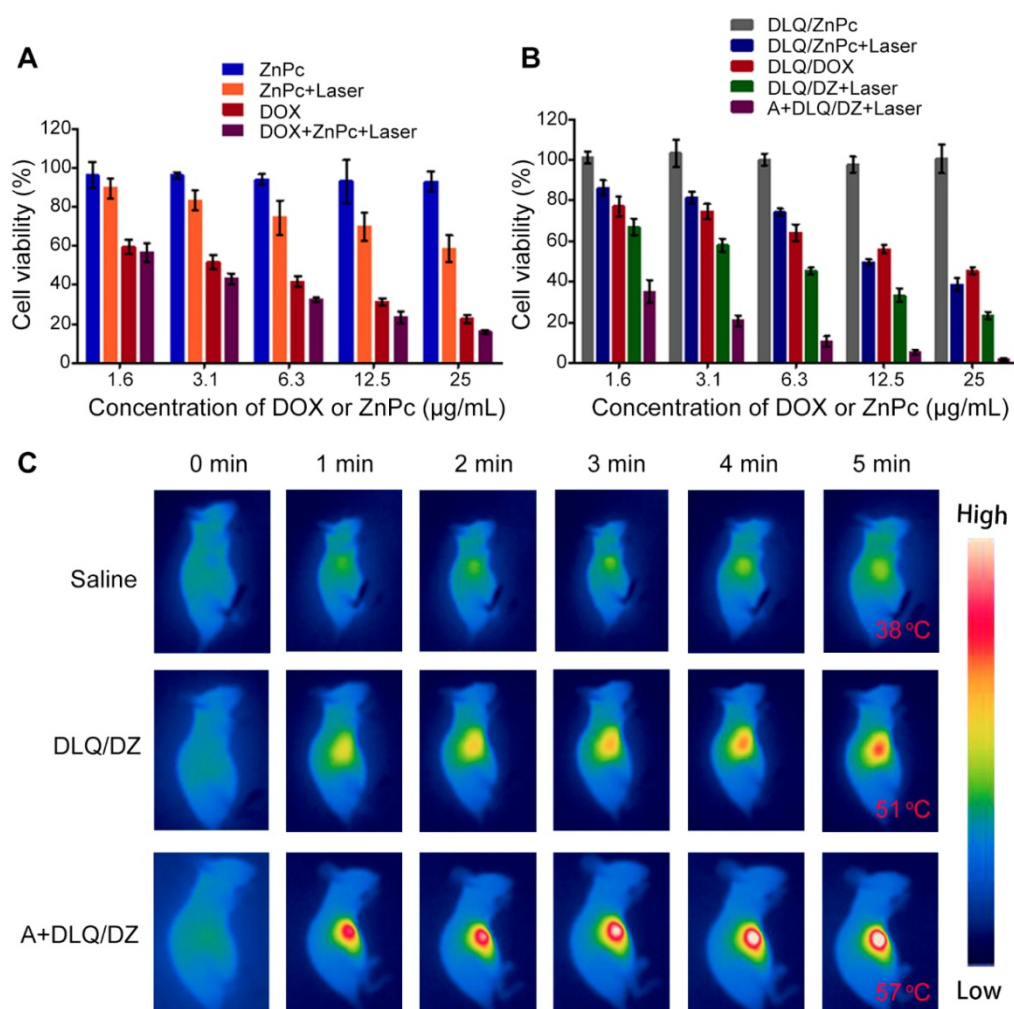


Figure 5. (A) Cytotoxicity of MCF-7 cells treated with ZnPc, ZnPc+Laser, DOX, and DOX+ZnPc+Laser. (B) Cytotoxicity of MCF-7 cells treated with DLQ/ZnPc, DLQ/ZnPc+Laser, DLQ/DOX, DLQ/DZ+Laser, and A+DLQ/DZ+Laser. Data are presented as the mean±SD (n=6). (C) Infrared thermal images of MCF-7 human tumor-bearing nude mice treated with saline, DLQ/DZ, and A+DLQ/DZ during the laser irradiations.

the body weight, ALT, AST (Figure 7C), and CK values (Figure 7D) in the DLQ/DZ and the A+DLQ/DZ groups demonstrated no significant differences compared to saline group, indicating their better biosafety characteristics. The superior biosafety of agents in the A+DLQ/DZ group was further

confirmed in the histological analysis of the major organ tissues (Figure 7E). Observed results showed no significant side effects in the A+DLQ/DZ group, supporting a high potential of this strategy in future clinical applications.

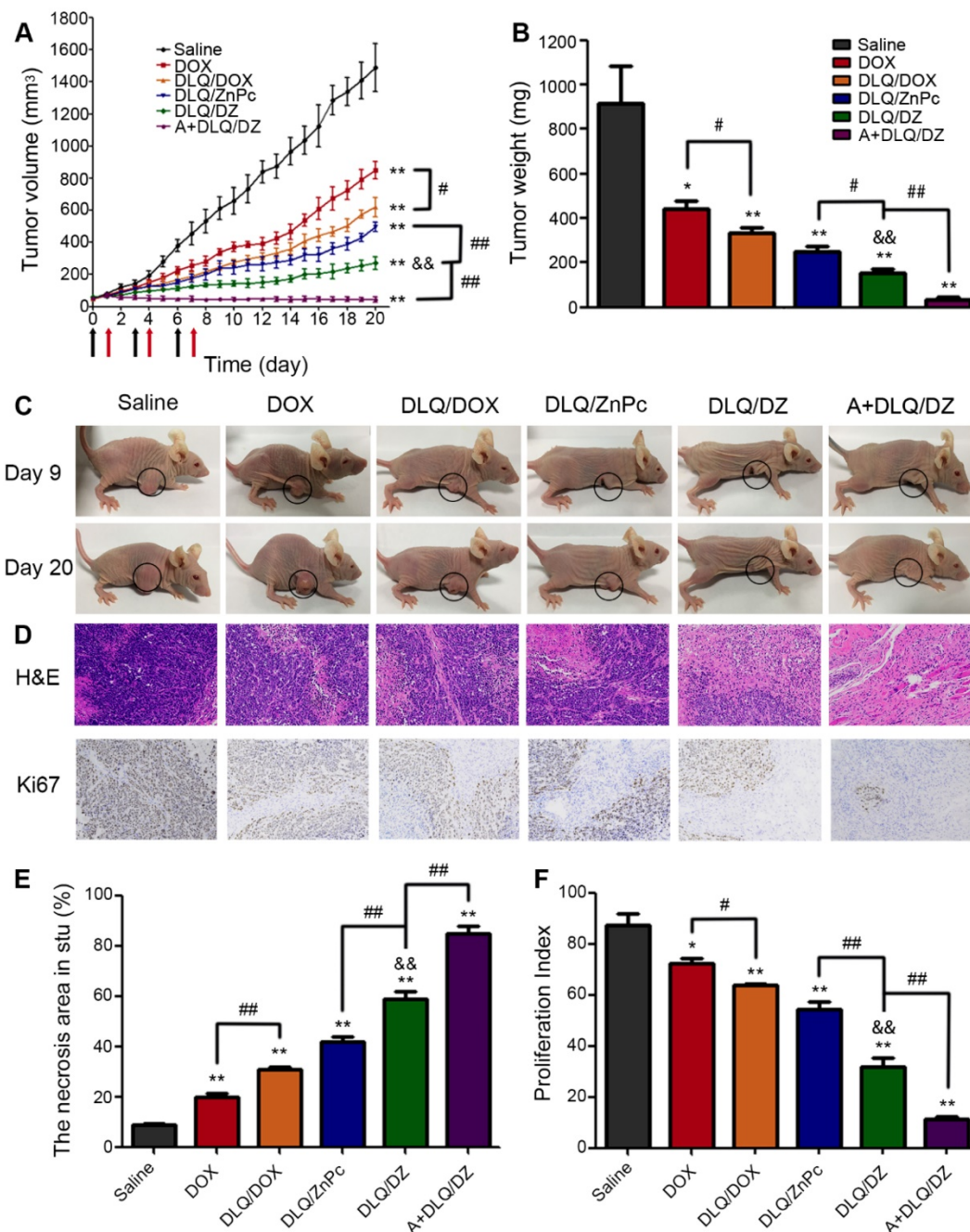


Figure 6. (A) The changes of tumor volume of MCF-7 human tumor-bearing nude mice from saline, DOX, DLQ/DOX, DLQ/ZnPc, DLQ/DZ, and A+DLQ/DZ treatment groups. Black arrows for tail vein administration, red arrows for laser irradiation. (B) Tumor weights of MCF-7 human tumor-bearing nude mice from different treatment groups at day 20. Data are represented as mean±SD (n=5) (C) Representative photographs of MCF-7 human tumor-bearing nude mice from different treatment groups at day 9 and 20. (D) H&E and Ki67 staining images (200-fold magnification) of the tumor tissues from different treatment groups. (E) The necrotic cells percentage of the tumor tissues after treatment. (F) The corresponding proliferating index of the tumor tissues in the Ki67 staining assay. Data are presented as the mean±SD (n=5). **P < 0.01, *P < 0.05 vs. the saline group, **P < 0.01 vs. the DLQ/DOX group, #P < 0.05, ##P < 0.01.

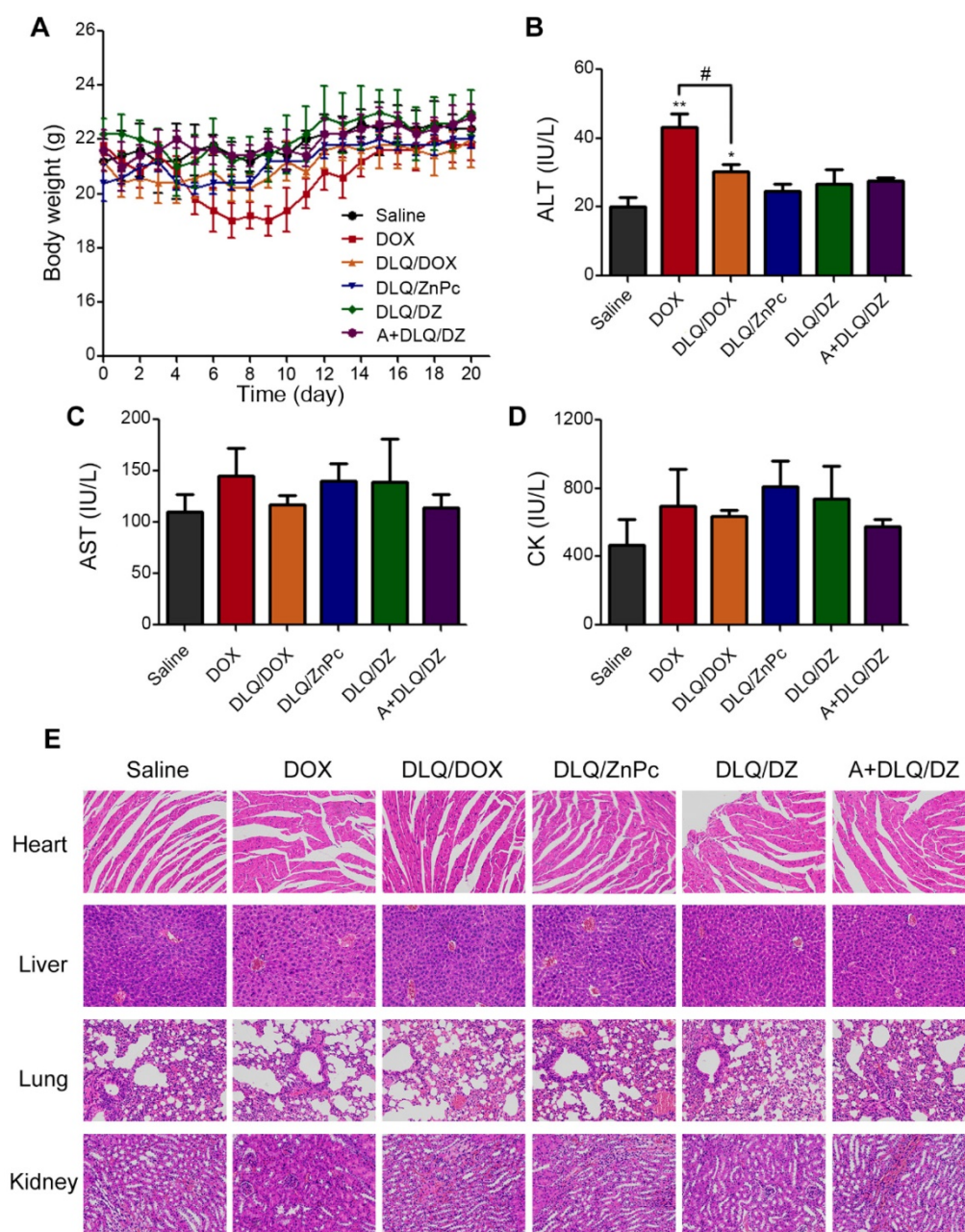


Figure 7. The body weight (A), ALT (B), AST (C) and CK (D) values of MCF-7 human breast tumor-bearing nude mice from saline, DOX, DLQ/DOX, DLQ/ZnPc, DLQ/DZ, and A+DLQ/DZ treatment groups. Data are represented as mean \pm SD (n=5). **P < 0.01, *P < 0.05 vs. the saline group, #P < 0.05. (E) H&E staining images (200-fold magnification) of the heart, liver, lung, kidney from different treatment groups.

Conclusion

In summary, we have successfully fabricated a nanocomposite for targeted chemo-photothermal combination therapy based on metabolic glycoengineering and bio-orthogonal copper-free click chemistry. The nano-system demonstrated superior tumor targeting ability and facilitated the precise co-delivery of both chemotherapeutic agents and photosensitizers. As a result, the orchestrated DLQ/DZ nanocomposites exerted a promising antitumor effect with an acceptable safety profile. This work provides insights into the improvement of

cancer therapies, particularly for tumors at anatomically superficial locations, such as breast cancers and melanomas. In addition, as successful combination therapy and efficient drug delivery are equally important for a variety of pathological treatments, the application of the bio-orthogonal click-targeting combination strategy used in this study may be extended beyond tumor treatment.

Abbreviations

PTT: photothermal therapy; NIR: near-infrared; ZnPc: zinc phthalocyanine; DOX: doxorubicin;

LMWH: low molecular weight heparin; Qu: quercetin; DBCO: dibenzocyclooctyne; Ac4ManNAz: tetraacetylated N-azidoacetyl-D-mannosamine; EPR: enhanced permeability and retention; LQ: low molecular weight heparin-quercetin conjugates; DL: dibenzocyclooctyne-low molecular weight heparin conjugates; DLQ: dibenzocyclooctyne-low molecular weight heparin-quercetin conjugates; CAC: critical aggregation concentration; DLQ/DZ: dibenzocyclooctyne-low molecular weight heparin-quercetin nanocomposites co-incorporating DOX and ZnPc; DLQ/DOX: DOX-loaded dibenzocyclooctyne-low molecular weight heparin-quercetin nanocomposites; DLQ/ZnPc: ZnPc-loaded dibenzocyclooctyne-low molecular weight heparin-quercetin nanocomposites; DLS: dynamic light scattering; TEM: transmission electron microscopy; DBCO-Cy5: Cy5-labeled dibenzocyclooctyne; DLQ-Cy5: Cy5-labeled dibenzocyclooctyne-low molecular weight heparin-quercetin nanocomposites; TCEP: tris (2-carboxyethyl)-phosphine; MTT: methyl thiazolyl tetrazolium; CI: combination index; ALT: alanine aminotransferase; AST: aspartate transaminase; CK: creatine kinase; NMP: N-methylpyrrolidone; EDC: 1-Ethyl-3 (3-dimethylaminopropyl) carbodiimide; NHS: N-hydroxysuccinimide; DMF: dimethylformamide; IR: tumor inhibition rate; SD: standard deviation.

Supplementary Material

Supplementary methods and figures.

<http://www.thno.org/v10p5305s1.pdf>

Acknowledgements

This work was supported by the National Natural Science Foundation of China (81773655), the "333" Project Talent Training Fund of Jiangsu Province (BRA2017432), the "Double First-Class" University Project (CPU2018GY14), the Open Project of Jiangsu Key Laboratory of Druggability of Biopharmaceuticals (JKLDBKF201702) and the Project Program of State Key Laboratory of Natural Medicines, China Pharmaceutical University (JKGQ201107). We are grateful to Dr. Sifei Han from Monash University, Australia, for discussion and the English editing of the manuscript.

Competing Interests

The authors have declared that no competing interest exists.

References

- Shi H, Sun Y, Yan R, Liu S, Zhu L, Liu S, et al. Magnetic semiconductor gd-doping cus nanoparticles as activatable nanoprobes for bimodal imaging and targeted photothermal therapy of gastric tumors. *Nano Lett.* 2019; 19: 937-47.

- Lyu Y, Cui D, Sun H, Miao Y, Duan H, Pu K. Dendronized semiconducting polymer as photothermal nanocarrier for remote activation of gene expression. *Angew Chem Int Ed Engl.* 2017; 56: 9155-9.
- Huang P, Rong P, Jin A, Yan X, Zhang MG, Lin J, et al. Dye-loaded ferritin nanocages for multimodal imaging and photothermal therapy. *Adv Mater.* 2014; 26: 6401-8.
- Chu KF, Dupuy DE. Thermal ablation of tumours: Biological mechanisms and advances in therapy. *Nat Rev Cancer.* 2014; 14: 199-208.
- Song J, Pu L, Zhou J, Duan B, Duan H. Biodegradable theranostic plasmonic vesicles of amphiphilic gold nanorods. *ACS Nano.* 2013; 7: 9947-60.
- Cheng L, Wang C, Feng L, Yang K, Liu Z. Functional nanomaterials for phototherapies of cancer. *Chem Rev.* 2014; 114: 10869-939.
- Hwang S, Nam J, Jung S, Song J, Doh H, Kim S. Gold nanoparticle-mediated photothermal therapy: Current status and future perspective. *Nanomedicine (Lond).* 2014; 9: 2003-22.
- Younis MR, Wang C, An R, Wang S, Younis MA, Li Z-Q, et al. Low power single laser activated synergistic cancer phototherapy using photosensitizer functionalized dual plasmonic photothermal nanoagents. *ACS Nano.* 2019; 13: 2544-57.
- Liao J, Li W, Peng J, Yang Q, Li H, Wei Y, et al. Combined cancer photothermal-chemotherapy based on doxorubicin/gold nanorod-loaded polymersomes. *Theranostics.* 2015; 5: 345-56.
- Yang J, Dai D, Lou X, Ma L, Wang B, Yang Y-W. Supramolecular nanomaterials based on hollow mesoporous drug carriers and macrocycle-capped cus nanogates for synergistic chemo-photothermal therapy. *Theranostics.* 2020; 10: 615-29.
- Peng J, Xiao Y, Li W, Yang Q, Tan L, Jia Y, et al. Photosensitizer micelles together with ido inhibitor enhance cancer photothermal therapy and immunotherapy. *Adv Sci (Weinh).* 2018; 5: 1700891.
- Wang C, Xu L, Liang C, Xiang J, Peng R, Liu Z. Immunological responses triggered by photothermal therapy with carbon nanotubes in combination with anti-ctla-4 therapy to inhibit cancer metastasis. *Adv Mater.* 2014; 26: 8154-62.
- Li Z, Huang H, Tang S, Li Y, Yu X-F, Wang H, et al. Small gold nanorods laden macrophages for enhanced tumor coverage in photothermal therapy. *Biomaterials.* 2016; 74: 144-54.
- Luo D, Carter KA, Miranda D, Lovell JF. Chemophototherapy: An emerging treatment option for solid tumors. *Adv Sci (Weinh).* 2017; 4: 1600106.
- Ma J, Chen D, Li Y, Chen Y, Liu Q, Zhou X, et al. Zinc phthalocyanine-soybean phospholipid complex based drug carrier for switchable photoacoustic/fluorescence image, multiphase photothermal/photodynamic treatment and synergetic therapy. *J Control Release.* 2018; 284: 1-14.
- Li W, Peng J, Yang Q, Chen L, Zhang L, Chen X, et al. A-lipoic acid stabilized dbx/ir780 micelles for photoacoustic/fluorescence imaging guided photothermal therapy/chemotherapy of breast cancer. *Biomater Sci.* 2018; 6: 1201-16.
- Zhang L, Zhang Y, Xue Y, Wu Y, Wang Q, Xue L, et al. Transforming weakness into strength: Photothermal-therapy-induced inflammation enhanced cytopharmaceutical chemotherapy as a combination anticancer treatment. *Adv Mater.* 2019; 31: 1805936.
- Tang W, Fan W, Wang Z, Zhang W, Zhou S, Liu Y, et al. Acidity/reducibility dual-responsive hollow mesoporous organosilica nanoplateforms for tumor-specific self-assembly and synergistic therapy. *ACS Nano.* 2018; 12: 12269-83.
- Tang W, Yang Z, Wang S, Wang Z, Song J, Yu G, et al. Organic semiconducting photoacoustic nanodroplets for laser-activatable ultrasound imaging and combinational cancer therapy. *ACS Nano.* 2018; 12: 2610-22.
- Fan W, Yung B, Huang P, Chen X. Nanotechnology for multimodal synergistic cancer therapy. *Chem Rev.* 2017; 117: 13566-638.
- Tang Q, Cheng Z, Yang N, Li Q, Wang P, Chen D, et al. Hydrangea-structured tumor microenvironment responsive degradable nanoplateform for hypoxic tumor multimodal imaging and therapy. *Biomaterials.* 2019; 205: 1-10.
- Luo D, Carter KA, Molins EAG, Straubinger NL, Geng J, Shao S, et al. Pharmacokinetics and pharmacodynamics of liposomal chemophototherapy with short drug-light intervals. *J Control Release.* 2019; 297: 39-47.
- Li Y, Deng Y, Tian X, Ke H, Guo M, Zhu A, et al. Multipronged design of light-triggered nanoparticles to overcome cisplatin resistance for efficient ablation of resistant tumor. *ACS Nano.* 2015; 9: 9626-37.
- Rao W, Deng Z-S, Liu J. A review of hyperthermia combined with radiotherapy/chemotherapy on malignant tumors. *Crit Rev Biomed Eng.* 2010; 38: 101-16.
- Dong X, Yin W, Zhang X, Zhu S, He X, Yu J, et al. Intelligent mos2 nanotheranostic for targeted and enzyme-/ph-/nir-responsive drug delivery to overcome cancer chemotherapy resistance guided by pet imaging. *ACS Appl Mater Interfaces.* 2018; 10: 4271-84.
- Liu Y, Bhattarai P, Dai Z, Chen X. Photothermal therapy and photoacoustic imaging via nanotheranostics in fighting cancer. *Chem Soc Rev.* 2019; 48: 2053-108.
- Han L, Hu L, Liu F, Wang X, Huang X, Liu B, et al. Redox-sensitive micelles for targeted intracellular delivery and combination chemotherapy of paclitaxel and all-trans-retinoid acid. *Asian J Pharm Sci.* 2019; 14: 531-42.
- Park JW, Hong K, Kirpotin DB, Colbern G, Shalaby R, Baselga J, et al. Anti-her2 immunoliposomes. *Clin Cancer Res.* 2002; 8: 1172-81.
- Denison TA, Bae YH. Tumor heterogeneity and its implication for drug delivery. *J Control Release.* 2012; 164: 187-91.

30. Laughlin ST, Baskin JM, Amacher SL, Bertozzi CR. In vivo imaging of membrane-associated glycans in developing zebrafish. *Science*. 2008; 320: 664-7.
31. Saxon E, Bertozzi CR. Cell surface engineering by a modified Staudinger reaction. *Science*. 2000; 287: 2007-10.
32. Wang H, Tang L, Liu Y, Dobrucka IT, Dobrucki LW, Yin L, et al. In vivo targeting of metabolically labeled cancers with ultra-small silica nanoconjugates. *Theranostics*. 2016; 6: 1467-76.
33. Koo H, Lee S, Na JH, Kim SH, Hahn SK, Choi K, et al. Bioorthogonal copper-free click chemistry in vivo for tumor-targeted delivery of nanoparticles. *Angew Chem Int Ed Engl*. 2012; 51: 11836-40.
34. Lee S, Yoon HI, Na JH, Jeon S, Lim S, Koo H, et al. In vivo stem cell tracking with imageable nanoparticles that bind bioorthogonal chemical receptors on the stem cell surface. *Biomaterials*. 2017; 139: 12-29.
35. Shim MK, Yoon HY, Ryu JH, Koo H, Lee S, Park JH, et al. Cathepsin b-specific metabolic precursor for in vivo tumor-specific fluorescence imaging. *Angew Chem Int Ed Engl*. 2016; 55: 14698-703.
36. Lee S, Koo H, Na JH, Han SJ, Min HS, Lee SJ, et al. Chemical tumor-targeting of nanoparticles based on metabolic glycoengineering and click chemistry. *ACS Nano*. 2014; 8: 2048-63.
37. Wang H, Wang R, Cai K, He H, Liu Y, Yen J, et al. Selective in vivo metabolic cell-labeling-mediated cancer targeting. *Nat Chem Biol*. 2017; 13: 415-24.
38. Qiu M, Sun H, Meng F, Cheng R, Zhang J, Deng C, et al. Lipopeptides: A novel and robust family of nano-vesicles capable of highly efficient encapsulation and tumor-targeted delivery of doxorubicin hydrochloride in vivo. *J Control Release*. 2018; 272: 107-13.
39. Mallick S, Thuy LT, Lee S, Park J II, Choi JS. Liposomes containing cholesterol and mitochondria-penetrating peptide (mpp) for targeted delivery of antimycin A to A549 cells. *Colloids Surf B Biointerfaces*. 2018; 161: 356-64.
40. Tian F, Dahmani FZ, Qiao J, Ni J, Xiong H, Liu T, et al. A targeted nanoplateform co-delivering chemotherapeutic and antiangiogenic drugs as a tool to reverse multidrug resistance in breast cancer. *Acta Biomater*. 2018; 75: 398-412.
41. Du L, Qin H, Ma T, Zhang T, Xing D. In vivo imaging-guided photothermal/photoacoustic synergistic therapy with bioorthogonal metabolic glycoengineering-activated tumor targeting nanoparticles. *ACS Nano*. 2017; 11: 8930-43.
42. Wang F, Sun Q, Feng B, Xu Z, Zhang J, Xu J, et al. Polydopamine-functionalized graphene oxide loaded with gold nanostars and doxorubicin for combined photothermal and chemotherapy of metastatic breast cancer. *Adv Healthc Mater*. 2016; 5: 2227-36.
43. Tewey KM, Rowe TC, Yang L, Halligan BD, Liu LF. Adriamycin-induced DNA damage mediated by mammalian DNA topoisomerase II. *Science*. 1984; 226: 466-8.
44. Li Y, Wu Y, Huang L, Miao L, Zhou J, Satterlee AB, et al. Sigma receptor-mediated targeted delivery of anti-angiogenic multifunctional nanodrugs for combination tumor therapy. *J Control Release*. 2016; 228: 107-19.
45. Hou L, Fan Y, Yao J, Zhou J, Li C, Fang Z, et al. Low molecular weight heparin-all-trans-retinoid acid conjugate as a drug carrier for combination cancer chemotherapy of paclitaxel and all-trans-retinoid acid. *Carbohydr Polym*. 2011; 86: 1157-66.
46. Torchilin V. Tumor delivery of macromolecular drugs based on the EPR effect. *Adv Drug Deliv Rev*. 2011; 63: 131-5.
47. Alexis F, Pridgen E, Molnar LK, Farokhzad OC. Factors affecting the clearance and biodistribution of polymeric nanoparticles. *Mol Pharm*. 2008; 5: 505-15.
48. He C, Hu Y, Yin L, Tang C, Yin C. Effects of particle size and surface charge on cellular uptake and biodistribution of polymeric nanoparticles. *Biomaterials*. 2010; 31: 3657-66.
49. Liu G, Ma J, Li Y, Li Q, Tan C, Song H, et al. Core-interlayer-shell Fe₃O₄@MSiO₂@lipid-peg-methotrexate nanoparticle for multimodal imaging and multistage targeted chemo-photodynamic therapy. *Int J Pharm*. 2017; 521: 19-32.
50. Han N, Wang Y, Bai J, Liu J, Wang Y, Gao Y, et al. Facile synthesis of the lipid bilayer coated mesoporous silica nanocomposites and their application in drug delivery. *Microporous Mesoporous Mater*. 2016; 219: 209-18.
51. Li T, Li C, Ruan Z, Xu P, Yang X, Yuan P, et al. Polypeptide-conjugated second near-infrared organic fluorophore for image-guided photothermal therapy. *ACS Nano*. 2019; 13: 3691-702.
52. Malinoff HL, Wicha MS. Isolation of a cell surface receptor protein for laminin from murine fibrosarcoma cells. *J Cell Biol*. 1983; 96: 1475-9.
53. Montet X, Funovics M, Montet-Abou K, Weissleder R, Josephson L. Multivalent effects of RGD peptides obtained by nanoparticle display. *J Med Chem*. 2006; 49: 6087-93.
54. Hong S, Leroueil PR, Majoros IJ, Orr BG, Baker JR, Banaszak Holl MM. The binding avidity of a nanoparticle-based multivalent targeted drug delivery platform. *Chem Biol*. 2007; 14: 107-15.
55. Mammen M, Choi S-K, Whitesides GM. Polyvalent interactions in biological systems: Implications for design and use of multivalent ligands and inhibitors. *Angew Chem Int Ed Engl*. 1998; 37: 2754-94.
56. Choi Y, Kim S, Choi M-H, Ryoo S-R, Park J, Min D-H, et al. Highly biocompatible carbon nanodots for simultaneous bioimaging and targeted photodynamic therapy in vitro and in vivo. *Adv Funct Mater*. 2014; 24: 5781-9.
57. Zhang M, Murakami T, Ajima K, Tsuchida K, Sandanayaka ASD, Ito O, et al. Fabrication of ZnPC/protein nanohorns for double photodynamic and hyperthermic cancer phototherapy. *Proc Natl Acad Sci U S A*. 2008; 105: 14773-8.
58. Xiong H, Du S, Ni J, Zhou J, Yao J. Mitochondria and nuclei dual-targeted heterogeneous hydroxyapatite nanoparticles for enhancing therapeutic efficacy of doxorubicin. *Biomaterials*. 2016; 94: 70-83.